



## In-operando elucidation of bimetallic CoNi nanoparticles during high-temperature CH<sub>4</sub>/CO<sub>2</sub> reaction



Bedour AlSabban<sup>a</sup>, Laura Falivene<sup>a</sup>, Sergey M. Kozlov<sup>a</sup>, Antonio Aguilar-Tapia<sup>a</sup>, Samy Ould-Chikh<sup>a</sup>, Jean-Louis Hazemann<sup>b</sup>, Luigi Cavallo<sup>a</sup>, Jean-Marie Basset<sup>a</sup>, Kazuhiro Takanabe<sup>a,\*</sup>

<sup>a</sup> King Abdullah University of Science and Technology (KAUST), KAUST Catalysis Center (KCC) and Physical Sciences and Engineering Division (PSE), Thuwal 23955-6900, Saudi Arabia

<sup>b</sup> Institut Néel, UPR 2940 CNRS, 38042 Grenoble Cedex 9, France

### ARTICLE INFO

#### Article history:

Received 25 February 2017

Received in revised form 5 April 2017

Accepted 30 April 2017

Available online 2 May 2017

#### Keywords:

Dry reforming of methane

Nickel

Cobalt

Bimetal

Carbon deposition

Kinetics

Density functional theory

*In-operando* X-ray absorption spectroscopy

### ABSTRACT

Dry reforming of methane (DRM) proceeds via CH<sub>4</sub> decomposition to leave surface carbon species, followed by their removal with CO<sub>2</sub>-derived species. Reactivity tuning for stoichiometric CH<sub>4</sub>/CO<sub>2</sub> reactants was attempted by alloying the non-noble metals Co and Ni, which have high affinity with CO<sub>2</sub> and high activity for CH<sub>4</sub> decomposition, respectively. This study was focused on providing evidence of the capturing surface coverage of the reactive intermediates and the associated structural changes of the metals during DRM at high temperature using *in-operando* X-ray absorption spectroscopy (XAS). On the Co catalysts, the first-order effects with respect to CH<sub>4</sub> pressure and negative-order effects with respect to CO<sub>2</sub> pressure on the DRM rate are consistent with the competitive adsorption of the surface oxygen species on the same sites as the CH<sub>4</sub> decomposition reaction. The Ni surface provides comparatively higher rates of CH<sub>4</sub> decomposition and the resultant DRM than the Co catalyst but leaves some deposited carbon on the catalyst surface. In contrast, the bimetallic CoNi catalyst exhibits reactivity towards the DRM but with kinetic orders resembling Co catalyst, producing negligible carbon deposition by balancing CH<sub>4</sub> and CO<sub>2</sub> activation. The *in-operando* X-ray absorption near edge structure (XANES) and extended X-ray absorption fine structure (EXAFS) measurements confirmed that the Co catalyst was progressively oxidized from the surface to the bulk with reaction time, whereas CoNi and Ni remained relatively reduced during DRM. Density functional theory (DFT) calculation considering the high reaction temperature for DRM confirmed the unselective site arrangement between Co and Ni atoms in both the surface and bulk of the alloy nanoparticle (NP). The calculated heat of oxygen chemisorption became more exothermic in the order of Ni, CoNi, Co, consistent with the catalytic behavior. The comprehensive experimental and theoretical evidence provided herein clearly suggests improvement to the catalyst design protocol by selecting the appropriate composition of Co-Ni alloy.

© 2017 The Authors. Published by Elsevier B.V. This is an open access article under the CC BY-NC-ND license (<http://creativecommons.org/licenses/by-nc-nd/4.0/>).

## 1. Introduction

The conversion of methane to syngas is a process of continuously gaining interest in the market for the natural gas and hydrogen industries [1–4]. The dry reforming of methane (DRM) is attractive because it utilizes a large amount of CO<sub>2</sub> (which may coexist in natural gas fields) into a mixture of higher-value compounds, with a tunable H<sub>2</sub>/CO ratio ~1 (CH<sub>4</sub> + CO<sub>2</sub> ⇌ 2CO + 2H<sub>2</sub>) and a concur-

rent reverse water gas shift (RWGS) reaction (H<sub>2</sub> + CO<sub>2</sub> ⇌ CO + H<sub>2</sub>O) [5–11]. To achieve high conversion, DRM must be performed at high temperature (700–900 °C) because of its high endothermicity ( $\Delta H^\circ = 246 \text{ kJ mol}^{-1}$ ). The high reaction temperature leads to metal sintering and carbon formation (coking), which cause catalyst deactivation [5–11]. A similar reaction, steam reforming of methane (SRM), can be performed industrially for a long period using relatively inexpensive Ni-based catalysts [1]. However, these catalysts produce a large amount of carbon on the catalyst surface (in whisker and encapsulating morphologies) under DRM, causing catalyst deactivation and reactor plugging (increase in back pres-

\* Corresponding author.

E-mail address: [kazuhiro.takanabe@kaust.edu.sa](mailto:kazuhiro.takanabe@kaust.edu.sa) (K. Takanabe).

sure) [5]. The commercialization of DRM therefore faces the serious challenge of completely suppressing carbon formation [4].

A number of studies have been reported on Ni catalysts for DRM [12–22]. Wei and Iglesia conducted a careful kinetic assessment of the forward conversion rate by taking approach-to-equilibrium without facing heat and mass transfer artifacts [15]. They reported that C–H bond activation of CH<sub>4</sub> is the sole kinetically relevant step for the overall DRM on a Ni/MgO catalyst at 600–700 °C (first-order with respect to CH<sub>4</sub> pressure) [15]. The reaction proceeds on a clean Ni surface, which is confirmed by the kinetic being independent of the co-reactant (CO<sub>2</sub>) and product (CO, H<sub>2</sub>, H<sub>2</sub>O) pressures. The concurrent RWGS is quasi-equilibrated under the investigated conditions. However, the kinetics do not provide information about undesired carbon formation, which occurs at a different time scale [15]. The mechanism proposed by Bengaard and Nørskov et al. based on DFT simulations together with experiments by Rostrup-Nielsen et al. suggested that the nucleation of unwanted carbon deposits is initiated by step sites of the Ni surface, which can be occupied by other elements, such as potassium, sulfur, and gold and other elements which explains their role of enhancement of selectivity [17,18]. In particular, the continuous addition of sulfur is performed industrially to suppress carbon formation during SRM (namely, SPARG process) [6]. Their study noted the critical role for the growth of carbon fiber/nanotube catalyzed by metal step sites [17,18]. It was suggested that the small size of nanoparticles (NPs) gives tolerance to carbon formation, which is consistent with DFT calculations, where surface graphite cannot form on small particles [18]. It is critical to consider the metal particle size and coordination number of surface metal sites to suppress carbon formation.

Co has gained attention as an active metal for DRM [23–26], despite its lower DRM rate than Ni [27]. The catalytic behavior of the Co catalyst is relatively distinct among the other group 8 metals. Depending on the metal loading, there is a clear trend where metallic Co is deactivated by carbon deposition (high loading) or metal oxidation (low loading) [23–25]. This trend was observed by varying the metal loading on both Co/Al<sub>2</sub>O<sub>3</sub> and Co/TiO<sub>2</sub> under various reaction conditions [23,24]. Metal oxidation was evidenced by the consumption of oxygen from CO<sub>2</sub> and inactive mixed oxide formation, such as CoAl<sub>2</sub>O<sub>4</sub> or CoTiO<sub>3</sub> [24,25], depending on the support. However, these findings suggest that there is kinetic competition between reduction (CH<sub>4</sub> activation) and oxidation (CO<sub>2</sub> activation) at the same surface. Although the Co-based catalyst has the potential to show high stability without causing carbon deposition for DRM, it still lacks accurate control of the kinetics through the design of the Co metal particle size because the reaction conditions, such as the reaction pressure [23,25], alter the appropriate catalyst to be used.

To further tune the reactivity of the metal, attempts have been made to produce stable catalysts by combining Co and Ni [27–48]. Because Ni is more reactive towards CH<sub>4</sub> decomposition, providing a reductive surface relative to monometallic Co, the resultant bimetallic CoNi alloy catalyst was proposed to tune the reactivity towards CH<sub>4</sub> and CO<sub>2</sub> activation, according to its metal composition [27–29]. Generally, a high Co content causes deactivation due to metal oxidation, while a high Ni content causes deactivation by carbon deposition, as reported for a TiO<sub>2</sub> supported catalyst at 750 °C [27–29]. For example, Nagaoka et al. found 0.5 wt.% Co<sub>9</sub>Ni<sub>1</sub>/TiO<sub>2</sub> provided relatively stable DRM performance, even at 2 MPa [29]. Similarly, the synergistic effect of the combination of Co and Ni was explained by the formation of a reducible alloy phase [28,33,34,39]. Recent literature has investigated the effects of the support, such as CeO<sub>2</sub>-ZrO<sub>2</sub>, known to provide active oxygen, which is generally claimed to suppress carbon deposition [36,39,40,47]. This approach, however, contradicts the kinetic findings of Wei and Iglesia for various metal catalysts, where the forward CH<sub>4</sub> turnover rate is independent of the type of support, including ZrO<sub>2</sub> and CeO<sub>2</sub>.

ZrO<sub>2</sub> [49]. None of the studies on bimetallic CoNi catalyst carefully analyzed the state and composition of the CoNi alloy on the surface and bulk in each NP and the resultant reactivity towards DRM. Despite the potential of the bimetallic CoNi catalysts for DRM, there is limited understanding of the composition and the degree of oxidation of the surface and the bulk of catalyst particles during DRM conditions. The mechanistic understanding of such system and associated kinetic analysis, to pin down the reaction intermediate is crucial to design stable catalysts. There is little information available in the literature regarding the catalyst structure monitored during the DRM catalysis at high temperatures.

This analysis of literature motivated us to investigate the precise control of the reactivity of bimetallic CoNi and to conduct *in-operando* characterization to capture its structural changes during the high-temperature DRM catalysis. The support selected in this study was ZrO<sub>2</sub>, which does not form mixed oxides with Co or Ni, ensuring a lack of thermodynamic driving force of the metal to be oxidized by the presence of the support, phenomena which occur on alumina or titania. Monometallic Co and Ni and bimetallic CoNi catalysts were prepared by an aqueous route known as homogeneous deposition precipitation (HDP) to reproducibly produce the fine-metal NPs with consistent size [50]. The high metal dispersion obtained was a key to improve surface/bulk ratio, to enhance the signals originating from surface structure. These metal NP catalysts were investigated using *in-operando* XAS supported by DFT calculations at high temperatures to fully understand the reactivity and susceptibility towards carbon formation and metal oxidation. By comparing the monometallic Co and Ni and bimetallic CoNi catalysts, direct experimental evidence is provided for the oxidation of Co under DRM condition, while CoNi and Ni maintain their reductive form. In turn, DFT calculations show that alloying Ni and Co allows one to control the oxophilicity of the catalyst in order to balance the kinetics of DRM. By including kinetic analysis, this study clearly demonstrates a technique to control the metal reactivity of CH<sub>4</sub> and CO<sub>2</sub> activation (redox capability) by metal identity (Co, Ni), as well as resultant inhibition of both carbon deposition and metal oxidation, thus explaining the stable DRM performance of the bimetallic CoNi catalyst.

## 2. Experimental and theoretical methods

### 2.1. Catalyst preparation

The ZrO<sub>2</sub> support (RC100, DAIICHI KIGENSO KAGAKU KOGYO CO., LTD) was first pretreated in static air at 900 °C to prevent sintering during DRM. Monometallic Co and Ni and bimetallic CoNi/ZrO<sub>2</sub> catalysts with intended total metal loadings of 0.5 wt.% (or 5 wt% for characterization purpose) were prepared by HDP. The required amount of an aqueous solution of nickel (II) chloride hexahydrate (NiCl<sub>2</sub>·6H<sub>2</sub>O, Sigma-Aldrich, 99.999%) and cobalt (II) chloride hexahydrate (CoCl<sub>2</sub>·6H<sub>2</sub>O, Sigma-Aldrich) was added after dissolving 2.5 g of urea (Sigma-Aldrich, ≥99.5%) in 100 mL of pure water. For the CoNi samples, 1:9, 5:5, 9:1 molar amounts of Co and Ni were used to achieve total metal loading of 0.5 wt.%. The sample with metal loading of ~4–5 wt% was synthesized for XRD measurements only. Typically, 1 g of heat-treated ZrO<sub>2</sub> support was added to the solution. Then, the mixture was heated to 90 °C for 1 h, causing the hydrolysis of urea, shifting the pH to ~10 and leading to the precipitation of metal hydroxide species. After cooling to room temperature, 100 mL of ethylene glycol (Sigma-Aldrich, 99%) was added, and the solution was heated to 150 °C for 3 h for stabilization. The resulting materials were filtered, washed with 300 mL of pure water and 100 mL of ethanol, and dried overnight at 100 °C.

## 2.2. Kinetic measurements

The DRM kinetic tests were conducted in a fixed-bed quartz microreactor (i.d. 4 mm) at atmospheric pressure (PID Eng & Tech). A tubular furnace with a temperature controller attached to a K-type thermocouple located at the center of the catalyst bed was used to control the temperature. The catalyst powders were pelletized and sieved to a particle size of 250–350 µm. To make the catalyst bed, for the Ni and CoNi samples, 5 mg of catalyst was diluted with 45 mg of ZrO<sub>2</sub> powder, and for the Co sample, 50 mg of catalyst was used without the dilution. The catalyst bed was supported using quartz wool. The catalyst was heated under flowing 20% H<sub>2</sub> in N<sub>2</sub> (AHG) at a flow rate of 100 mL min<sup>-1</sup> at 800 °C and then for 1 h at a ramp rate of 10 °C min<sup>-1</sup>. Different partial pressures of CH<sub>4</sub> (99.9999%, AHG), CO<sub>2</sub> (99.9999%, AHG), and N<sub>2</sub> (99.9999%, AHG) were introduced into the reactor by regulating the flow rates by mass flow controllers (F-200 series, Bronkhorst). The reactants and products were continuously monitored using an on-line micro gas chromatograph (Varian, 490-GC) equipped with two thermal conductivity detectors, a Molecular Sieve 5A column and a Porapak Q column.

## 2.3. In-operando X-ray absorption spectroscopy

To study the structural differences between monometallic Co and Ni and bimetallic CoNi catalyst under relevant DRM conditions, a dedicated cell for *in-operando* XAS was designed as a plug-flow reactor. The complete set-up is now permanently installed on the CRG-FAME beamline (BM30B) at the European Synchrotron Radiation Facility (ESRF) in Grenoble. Briefly, the reactor is tubular and fabricated from vitreous carbon. The carbon reactor was confirmed to be inert under DRM conditions by a blank test. The heating element design is based on Tamura et al. [51]. It consists of placing the reactor in a molybdenum tube that is heated to the experimental temperature with a resistive molybdenum metallic wire. Since the sample is at the center of the heating zone, the heating elements have three 5 mm diameter apertures to operate the cell in transmission and/or fluorescence detection modes. The regulation of the reaction temperature was performed by a type K thermocouple placed inside the reactor as close as possible to the sample. A series of automated mass flow controllers were used to deliver the various gas mixtures to the reactor, and the gas composition was monitored by an EcoCat-P portable mass spectrometer system from ESS equipped with two capillaries for on-line analysis of the reactor outlet and a bypass line. A vector gas mixture of 1% Ar in He was used as an internal standard to quantify the variation of the flow rate due to the stoichiometry of the reforming reaction. The gas distribution system was also fitted with a four-way valve to allow the preparation of the gas mixture in the bypass line before starting the reaction. This was performed using mass spectrometry and by monitoring the stabilization of the current intensities corresponding to *m/z* = 15 (*I(CH<sub>4</sub>)<sub>i</sub>*), *m/z* = 44 (*I(CO<sub>2</sub>)<sub>i</sub>*), and *m/z* = 40 (*I(Ar)<sub>i</sub>*) for CH<sub>4</sub>, CO<sub>2</sub>, and Ar gases, respectively. The amounts of reacted CH<sub>4</sub> and CO<sub>2</sub> were assessed by following the current intensities corresponding to *m/z* = 15 (*I(CH<sub>4</sub>)<sub>f</sub>*) and *m/z* = 44 (*I(CO<sub>2</sub>)<sub>f</sub>*) at the reactor outlet. Thus, the conversions of methane (*X(CH<sub>4</sub>)*) and carbon dioxide (*X(CO<sub>2</sub>)*) were calculated during the reaction using Eqs. (1) and (2):

$$X(\text{CH}_4)[\%] = \left\{ 1 - \left( \frac{I(\text{CH}_4)_f}{I(\text{CH}_4)_i} \right) \left( \frac{I(\text{Ar})_i}{I(\text{Ar})_f} \right) \right\} \times 100 \quad (1)$$

$$X(\text{CO}_2)[\%] = \left\{ 1 - \left( \frac{I(\text{CO}_2)_f}{I(\text{CO}_2)_i} \right) \left( \frac{I(\text{Ar})_i}{I(\text{Ar})_f} \right) \right\} \times 100 \quad (2)$$

The measurements were conducted using 50 mg of the sieved catalyst. First, XAS spectra were recorded under inert gas at room temperature to characterize the initial state of the catalyst. Then, a flow of 4% H<sub>2</sub>/He was introduced into the reactor at a flow rate of 100 mL min<sup>-1</sup>, which was heated to 750 °C at 10 °C min<sup>-1</sup> and maintained for 1 h. During this reduction process, XANES spectra were recorded continuously to observe the changes in the metal oxidation state. After the reduction step, the reactor was purged with the gas vector at 750 °C. The reaction mixture of 1:1:8 CO<sub>2</sub>:CH<sub>4</sub>:(1% Ar/He) was subsequently introduced at a flow rate of 100 mL min<sup>-1</sup> (GHSV = 120 L h<sup>-1</sup> g<sup>-1</sup>). The structure of the metal NPs was initially followed by XANES spectroscopy to capture the structural changes. After the initial transition, detailed EXAFS spectra were acquired. The reactions were kept for 10 h, and the last three EXAFS spectra out of approximately fifteen were merged to compare the final state of the catalysts. The initial conversion and the deactivation rate were identical to those measured in our lab-based microreactors, which was a convincing qualification of the XAS cell. Spectra were recorded either in fluorescence (DRM catalysts) or transmission (references) mode at the Co K-edge (7.709 keV) and Ni K-edge (8.333 keV), depending on the catalyst. For the bimetallic CoNi catalyst, the Co K-edge was followed during the reduction step and the DRM, while only the final state of Ni was recorded at the end of each procedure.

All XAS data were analyzed using the HORAE package, a graphical interface to the AUTOBK and IFEFFIT code [52]. The XANES and EXAFS spectra were obtained after performing standard procedures for pre-edge subtraction, normalization, polynomial removal, and wavevector conversion. The amplitude factor (S<sub>0</sub><sup>2</sup>) was fitted to the EXAFS spectra recorded for Co and Ni metallic foil, the unit cell being hexagonal (P6<sub>3</sub>/mmc) for Co and cubic (Fm<sup>3</sup>m) for Ni. A k-range of [3.3; 12] Å<sup>-1</sup> and R-range of [0.85; 5.1] Å were selected and fitted using single scattering paths and multiple scattering paths calculated from the metallic Co and Ni crystal structures (Fig. S1 and Table 1) [53]. The parametrization of the latter scattering paths was as follows: a single shift of energy was used, all amplitudes were adjusted by the amplitude reduction factor (S<sub>0</sub><sup>2</sup>), the variation of distances was calculated by adjusting the cell parameters of the considered unit cell, each single scattering path was fitted with an independent mean square displacement parameter, and the disorder for multiple scattering paths (triangular and collinear pathways) was modeled by linear combinations of the mean square displacement parameters used for the single scattering paths. S<sub>0</sub><sup>2</sup> were determined to be 0.87 ± 0.04 and 0.83 ± 0.07 for Co and Ni, respectively. The fits of the EXAFS spectra for the metallic catalysts were limited to a first shell analysis (R-range of [0.85; 2.7] Å) due to the lesser data quality recorded on powdered materials at high temperature (selected k-range: [2.7; 8.1] Å<sup>-1</sup>). First shell analysis for the monometallic and bimetallic catalysts was performed using a cubic unit cell since the Co transition from the *hcp* to *fcc* phase occurs above 450 °C [54–56]. Bond length distribution should ideally be modeled using a cumulant expansion to account for the anharmonic vibrations which are relevant at high temperature. Since the number of independent parameters was restrained by the available k-range, the harmonic approximation had to be used instead. The comparison of sample remained valid as the error due to the harmonic approximation was systematic and identical for all spectra recorded at the same temperature. For the particular case of the bimetallic catalyst, the model selected to fit the Co and Ni K-edge EXAFS spectra assumes a relatively homogenous mixture of Co and Ni atoms within the NP: a unique mean square displacement parameter and a unique path length were used for the parametrization of both the Co → Ni and Ni → Co scattering paths. The validity of the latter assumption was proved both experimentally via elemental mappings acquired by TEM and theoretically

**Table 1**

Parameters extracted from the fits of *in-operando* EXAFS data for Ni/ZrO<sub>2</sub>, Co/ZrO<sub>2</sub> and bimetallic CoNi/ZrO<sub>2</sub> catalysts reduced at 750 °C with a 4% H<sub>2</sub>/He gas flow and after 10 h of DRM. N, degeneracy of the scattering path; R, the half path length; σ<sup>2</sup>, mean square displacement parameter; ΔE, inner potential correction; R-factor, residual factor (underlined characters denote fixed parameters).

Operating conditions	Catalyst	Scattering paths	N	R [Å]	σ <sup>2</sup> [Å <sup>2</sup> ]	ΔE [eV]	R-factor
4% H <sub>2</sub> /He 750 °C 1 h	Ni/ZrO <sub>2</sub>	Ni → Ni	9 ± 2	2.47 ± 0.02	0.019 ± 0.003	-6 ± 2	$6 \times 10^{-3}$
	Co/ZrO <sub>2</sub>	Co → Co	7 ± 4	2.44 ± 0.05	0.015 ± 0.006	-9 ± 6	$4 \times 10^{-2}$
	CoNi/ZrO <sub>2</sub>	Ni → Ni	9 ± 1	2.45 ± 0.01	0.018 ± 0.002	-9 ± 1	$1 \times 10^{-2}$
		Co → Co	8 ± 2			-8 ± 2	
DRM 750 °C 10 h	Ni/ZrO <sub>2</sub>	Ni → Ni	11 ± 2	2.46 ± 0.01	0.019 ± 0.003	-7 ± 2	$4 \times 10^{-3}$
	Co/ZrO <sub>2</sub>	Co → Co	7 ± 4	2.45 ± 0.04	0.020 ± 0.008	-9 ± 5	$1 \times 10^{-3}$
		Co → O	1.2 ± 0.6	1.95 ± 0.04	<u>0.006</u>		
	CoNi/ZrO <sub>2</sub>	Ni → Ni	10 ± 1	2.47 ± 0.01	0.017 ± 0.002	-8 ± 1	$5 \times 10^{-3}$
		Co → Co	7 ± 1			-8 ± 1	
		Co → O	0.7 ± 0.2	1.97 ± 0.03	<u>0.006</u>	-8 ± 1	

via DFT calculations (*vide infra*). No additional Co → Ni and Ni → Co scattering paths were introduced in the model since the backscattering amplitude and total scattering phase shift are too close for Co and Ni atoms. However, the amplitude parameters were refined separately to highlight the possible segregation of one of the metals during the catalytic reaction. Finally, oxygen coverage calculation is detailed in Supporting Information.

#### 2.4. Characterization

Inductively coupled plasma (ICP) analysis was performed using a Varian 72 ES ICP-OES (Agilent Technologies) to measure the exact metal content. Digestion of the materials was performed in an ETHOS1 microwave digestion milestone.

Scanning transmission electron microscopy (STEM) was performed on a Titan G 60–300 ST electron microscope at an accelerating voltage of 300 kV using a Gatan STEM detector (model 806) to allow dark field imaging. The elemental compositions of the samples were characterized by the simultaneous acquisition of spectra by electron energy loss spectroscopy (EELS) and energy dispersive X-ray fluorescence spectrometry (EDX); the Ni L<sub>2,3</sub>-edge, Co L<sub>2,3</sub>-edge and Zr K<sub>α</sub> fluorescence lines were selected to build the chemical maps. A small camera length of 38 mm was used for imaging and elemental mapping to enhance the signal-to-noise ratio of the EELS spectra.

Powder XRD patterns were measured using a Bruker D8 Advanced A25 diffractometer in Bragg-Brentano geometry equipped with a Cu tube (Cu-K<sub>α</sub> radiation,  $\lambda=1.5406\text{ \AA}$ ). A linear position-sensitive detector (opening 2.9°) was operated at 40 kV and 40 mA. X-ray diffractometer data were collected in the range of  $2\theta=20\text{--}80^\circ$  under continuous scanning mode.

The amount of carbon deposited on the catalysts after DRM was quantified by temperature-programmed oxidation (TPO) under 1% O<sub>2</sub>/He. Ten milligrams of the spent catalyst was transferred to a tubular quartz reactor heated to 800 °C at a linear ramping rate of 10 °C min<sup>-1</sup>. The deposited carbon was oxidized to CO and CO<sub>2</sub>, which was converted to CH<sub>4</sub> by a methanizer, and this CH<sub>4</sub> was analyzed by a GC (Shimadzu GC-8A) equipped with a flame ionization detector (FID).

#### 2.5. Theoretical method

VASP software [57] was used to perform periodic calculations with the rPBE exchange-correlation functional, which is particularly suitable for studies of adsorption on metal surfaces [58]. The eigenstates of the valence electrons were calculated using plane-wave basis sets with a cutoff of 400 eV. First-order Methfessel-Paxton smearing of 0.1 eV was applied to the occupation numbers [59]. The presence of core electrons was accounted for via the projector augmented wave technique [60]. All calcu-

lations, except for the gas-phase CO species, were performed in the spin-polarized fashion. For Ni and Co systems as well as for selected configurations of Co-Ni alloys with adsorbates five adjacent magnetic states were explored to find the lowest energy spin configuration. Monkhorst-Pack meshes of k-points (5 × 5 × 1) were used to sample the reciprocal space in the slab calculations. NP model calculations were performed at  $\Gamma$ -point in the reciprocal space. Geometry optimization was performed until the forces on all atoms were less than 0.2 eV nm<sup>-1</sup>.

The adsorption energies of the CO species were calculated as follows:  $E_{\text{ads}}[\text{CO}] = -(E[\text{CO}/\text{substrate}] - E[\text{substrate}] - E[\text{CO}])$ , where  $E[\text{CO}/\text{substrate}]$  is the energy of a CO molecule adsorbed on the surface,  $E[\text{CO}]$  is the energy of the respective gas-phase species and  $E[\text{substrate}]$  is the energy of the substrate, i.e. the metallic slab used in the calculations. The energies of dissociative O adsorption were calculated as follows:  $E_{\text{ads}}[\text{O}] = -(E[\text{O}/\text{substrate}] - E[\text{substrate}] - E[\text{O}_2]/2)$ , where  $E[\text{O}/\text{substrate}]$  is the energy of an O atom adsorbed on the surface and  $E[\text{O}_2]$  is the energy of a triplet gas-phase O<sub>2</sub> molecule. Finally, the energies of C adsorption are calculated as follows:  $E_{\text{ads}}[\text{C}] = -(E[\text{C}/\text{substrate}] - E[\text{substrate}] - E[\text{graphene}])$ , where  $E[\text{C}/\text{substrate}]$  is the energy of a C atom adsorbed on the surface and  $E[\text{graphene}]$  is the energy per C atom of a graphene sheet in the gas phase. With these definitions, positive adsorption energies correspond to exothermic adsorption.

The surfaces were modeled using a 6 layer p(4 × 4) periodic slab hexagonal supercell of 997 × 997 pm for Ni (experimental Ni–Ni distance of 249 pm), 1002 × 1002 pm for Co (experimental Co–Co distance of 251 pm) and 999 × 999 pm for CoNi based on the average of the cell parameters of Co and Ni. The separation between adjacent slabs exceeded 1 nm.

### 3. Results and discussion

#### 3.1. Metal composition of the reduced samples

The ICP results for determining the actual metal loading are compiled in Table 2. The same loading ranges of 0.35–0.45 wt.% were identified for monometallic Co and Ni and bimetallic CoNi samples. This low loading was intentionally applied to maintain small and similar particle sizes (high surface to bulk ratio), to be able to capture the surface structural changes in the XAS measurements (*vide infra*). These metal particles were visualized by TEM measurement, and the images of the reduced samples are shown in Fig. 1 and Figs. S2, SI. The TEM images show that the ZrO<sub>2</sub> particles ranged from 20 to 100 nm. Generally, high metal dispersion with a narrow size distribution was obtained, resulting in 4–10 nm, regardless of the samples (Table 2). Accordingly, the metal surface quantities (in  $\mu\text{mol g}^{-1}$ ) and metal dispersion (%D) were calculated based on the average particle size by TEM assuming a hemispherical particle shape and are shown in Table 2. Similar dispersions

**Table 2**

ICP results and metal particle size observed by TEM for CoNi/ZrO<sub>2</sub> catalysts with different Co/Ni ratios reduced at 750 °C. The surface area of the metal and metal dispersion were estimated from particle size based on the hemispherical assumption.

Catalyst	Metal loading measured by ICP (wt.%)		Average particle size observed by TEM (nm)	Metal surface area ( $\mu\text{mol g}^{-1}$ )	Metal dispersion (%)
	Ni	Co			
Ni/ZrO <sub>2</sub>	0.35	—	6.3	9.3	16
Ni <sub>9</sub> Co <sub>1</sub> /ZrO <sub>2</sub>	0.38	0.04	5.9	11.9	17
CoNi/ZrO <sub>2</sub>	0.22	0.22	5.1	14.4	20
Co <sub>9</sub> Ni <sub>1</sub> /ZrO <sub>2</sub>	0.04	0.36	4.6	14.3	21
Co/ZrO <sub>2</sub>	—	0.45	5.6	13.2	17

of 16–20% were obtained among the three samples. In addition, elemental mappings by STEM-EELS/EDX of ten different regions of the CoNi/ZrO<sub>2</sub> sample demonstrated that the location of Co always overlapped well with that of Ni, suggesting the formation of CoNi alloy (Fig. 1 and Figs. S3, SI). No segregation of Co-Ni phase was evident from the STEM images.

The XRD patterns for the samples are shown in Figs. S4, SI. Only monoclinic ZrO<sub>2</sub> phase was identified for all samples, and no detectable peaks for the metal phase were measured in the XRD patterns due to the low metal quantity and small metal particle size. Higher loading samples (4–5 wt% loading) were therefore synthesized and XRD patterns were recorded to capture information of the CoNi metallic states. The results are shown in Figs. S5, SI. Each catalyst showed only one peak corresponding to metallic (111) diffraction, which was shifted according to the monometallic Co (44.22°) to monometallic Ni (44.51°) when varying Co:Ni ratios from 1:9, 1:1 to 9:1. This is indicative of alloy form of Co and Ni after the reduction [27]. Together with STEM-EELS/EDX mapping, XRD results suggest that CoNi are in the form of a homogeneous alloy.

In-operando XAS was used to investigate the structural differences among the bimetallic CoNi catalyst and its monometallic counterparts before DRM measurements. The XANES spectra for the Co and Ni K-edge, as shown in Fig. 2, are similar for all catalysts after synthesis. The systematic occurrence of a weak peak in the pre-edge region due to the 1s → 3d quadrupolar transitions and the intense white line are characteristic of an oxidized state of Co and Ni, both sitting in octahedral environments [61,62]. This is further

confirmed by examining the EXAFS spectra and their corresponding Fourier transforms, which display two scattering paths that are easily attributed to an oxygen and a metal shell (an Ni and/or Co atom). The peak amplitude corresponding to the metal shell is also much weaker than the oxide references (Fig. S6). Thus, the materials obtained after synthesis present two key features: i) a local structural order that is qualitatively identical for both types of metal centers, ii) a disordered or amorphous state of a metal oxide. The HDP method enabled the preparation of similar material structures starting either from Ni or Co precursors or an equimolar mixture of both metals.

After treatment of the catalysts with a 4% H<sub>2</sub>/He gas flow, all XANES spectra measured at 750 °C depicted an increase in the pre-edge peak intensity and the disappearance of the white line previously observed for the starting materials. Comparison of the XANES and EXAFS spectra taken at 750 °C with the reference spectra supports the formation of metallic NPs in all catalysts (Fig. S6). The quantitative analysis of the EXAFS spectra is shown in Table 1 and Fig. S7. The first coordination spheres of the Ni and Co catalysts are fitted with 9 ± 2 Ni atoms at 2.47 ± 0.02 Å and 7 ± 4 Co atoms at 2.44 ± 0.05 Å, respectively. The mean square displacement parameters for all fits are in the range of ≈ 1.5–1.9 × 10<sup>-2</sup> Å<sup>2</sup>, as expected for a high-temperature reaction. It was not possible to include metal–oxygen scattering paths in the fits, which indicates the complete reduction of all metal atoms. The coordination number of the shortest metal–metal bond determined by EXAFS is dependent on the size and shape of the metal NPs [63]. Generally, the smaller the size of the metal NPs is, the lower the average coordination number becomes because of the high proportion of low-coordinated surface atoms. The relationship between the coordination numbers and their particle size is shown in Fig. S8 [64]. Using this correlation, the obtained coordination numbers by EXAFS corresponded to 1 nm size for Co and Ni NPs, in contrast to the average particle sizes (≈ 5–6 nm) observed by TEM imaging (Fig. 1). Furthermore, the cell parameters calculated for the two monometallic catalysts (3.45 Å for Co and 3.49 Å for Ni) were also smaller than the reported values at 750 °C (> 3.54 Å) [65–68]. The discrepancy between the EXAFS spectroscopy and other characterization techniques was first reported for Ni and Cu NPs by Apai et al. [69] and was later interpreted in detail by Clausen et al. [70,71]. These authors used molecular dynamics simulations to show that the surface atoms in NPs move in a much more anharmonic potential than the bulk atoms, especially for the first-row transition metals. Because the anharmonicity becomes increasingly important for the smallest particles and at high temperatures, the approximation of the thermal vibration as harmonic in the standard EXAFS analysis formalism introduces significant underestimation in the apparent bond distance (up to 4%) and in the coordination number (up to 20–25%) [71,72]. Nevertheless, the absolute value of the coordination number and the distance have to be considered with care; their relative evolution from one material to another at the same temperature remains useful for the present study. Considering the bimetallic CoNi catalyst, the first coordination spheres of Co and

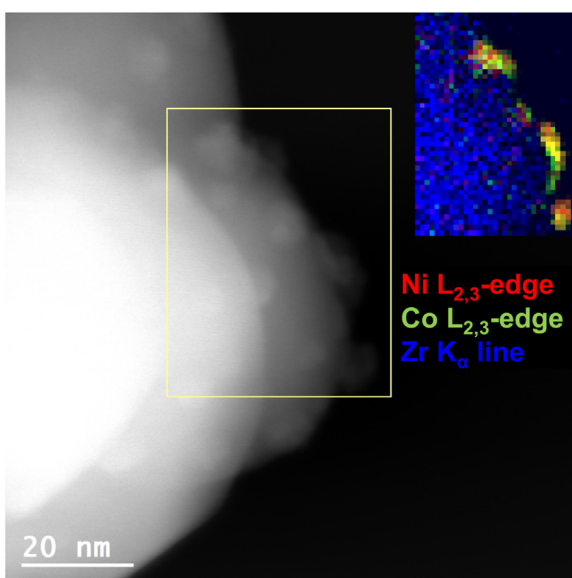


**Fig. 1.** Dark field STEM image of CoNi bimetallic nanoparticles supported on ZrO<sub>2</sub>. The inset shows the elemental mapping corresponding to the yellow rectangle region extracted from a STEM-EELS/EDX acquisition.

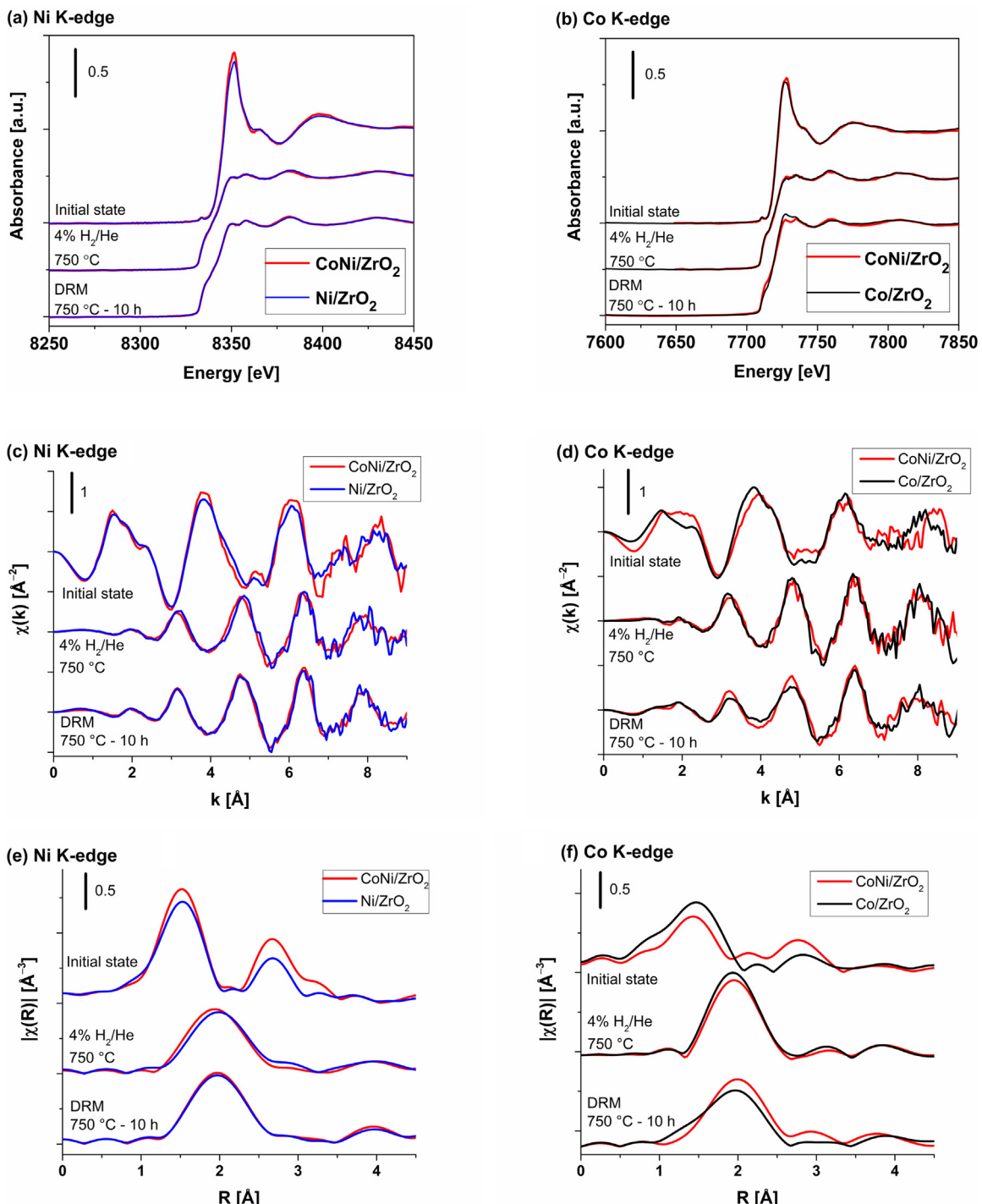


**Fig. 2.** Comparison of the *in-operando* XANES spectra, EXAFS  $k^2\chi(k)$  functions and their related Fourier transforms for  $\text{Ni/ZrO}_2$ ,  $\text{Co/ZrO}_2$  and bimetallic  $\text{Co}_1\text{Ni}_1/\text{ZrO}_2$  catalysts as synthesized (measured at room temperature), reduced at 750 °C with a 4%  $\text{H}_2/\text{He}$  gas flow and after 10 h of DRM: (left) Ni K-edge and (right) Co K-edge.

Ni are, respectively, fitted with  $9 \pm 1$  and  $8 \pm 2$  metal atoms at the same distance of  $2.45 \pm 0.01 \text{ \AA}$ . Considering the statistical accuracy, the coordination number of the metal–metal bonds for Co and Ni atoms are comparable and thus do not highlight a specific segregation of one particular metal atom towards the NP surface. The CoNi NPs were formed on the zirconia surface most probably as a homogenous alloy.

Since the experimental techniques used lack atomic resolution, we performed DFT simulations aimed to elucidate the availability of the different active sites on the surface of the reduced CoNi par-

ticles. Although Co and Ni NPs have an unequivocally determined structure, CoNi NPs at the reaction temperature may exhibit various instantaneous structures that differ not only by atomic displacement but also by chemical ordering. The latter describes the relative arrangement of Co and Ni atoms within an alloy with a fixed lattice. To generate a representative structure of CoNi NPs, the method of topological energy is applied [72]. Briefly, the proposed method approximates the NP energy using a topological energy expression that depends only on the most essential structural features, namely, the number of Co or Ni atoms on the corner, edge and terrace sites,

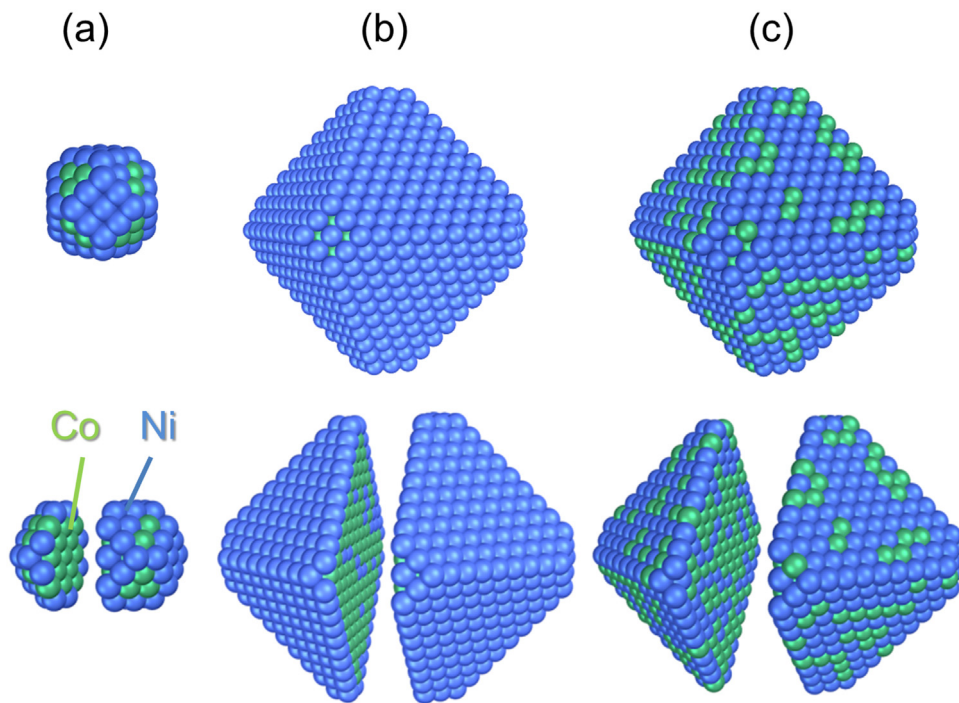


**Fig. 3.** (a) The configuration of cuboctahedral fcc  $\text{Co}_{58}\text{Ni}_{58}$  with the lowest obtained DFT energy, and the representative chemical ordering of truncated octahedral fcc  $\text{Co}_{719}\text{Ni}_{720}$  NP at (b) absolute zero and (c) 1000 K. All nanoparticles below are split in half to display the interior region. Co and Ni atoms are displayed as blue and green spheres, respectively.

as well as the number of Co-Ni bonds in the NP. This method was shown to yield results in line with experimental observations for very different Pd-based alloys [73], as well as for PtCo [74,75], PtSn [76], and CuNi [77].

In line with the established protocol [73], we performed DFT calculations of 39 cuboctahedral 1.3 nm large  $\text{Co}_{58}\text{Ni}_{58}$  NPs with different arrangement of Co and Ni atoms. Then we fitted the parameters  $\varepsilon_i$  in the topological energy expression to achieve the best agreement between DFT energies,  $E_{\text{DFT}}$ , and topologic energies,  $E_{\text{TOP}}$ :

$$E_{\text{TOP}} = E_0 + \varepsilon_{\text{BOND}}^{\text{Ni-Co}} N_{\text{BOND}}^{\text{Ni-Co}} + \varepsilon_{\text{CORNER}}^{\text{Co}} N_{\text{CORNER}}^{\text{Co}} + \varepsilon_{\text{EDGE}}^{\text{Co}} N_{\text{EDGE}}^{\text{Co}} \\ + \varepsilon_{\{100\}}^{\text{Co}} N_{\{100\}}^{\text{Co}} + \varepsilon_{\{111\}}^{\text{Co}} N_{\{111\}}^{\text{Co}}$$

In this formula  $N_{\text{BOND}}^{\text{Ni-Co}}$  is the number of heteroatomic bonds in the NP, and  $N_X^{\text{Co}}$  is the number of Co atoms occupying sites of type X. In turn, the fitted parameters  $\varepsilon$  (called descriptors) have clear physical meanings. For example,  $\varepsilon_{\text{BOND}}^{\text{Ni-Co}}$  is the energy of a heteroatomic bond,  $\varepsilon_{\{100\}}^{\text{Co}}$  is the segregation energy of a Co atom on a {100} facet of the nanoparticle (given that  $N_{\text{BOND}}^{\text{Ni-Co}}$  remains constant). Finally,  $E_0$  is a constant required for the fitting.

According to the performed fitting the formation of heteroatomic bonds was calculated to be slightly exothermic,  $\varepsilon_{\text{BOND}}^{\text{Ni-Co}} = -0.2 \text{ kJ mol}^{-1}$ . On the contrary, the energies of Co segregation on the nanoparticle surface were calculated to be endothermic,  $\varepsilon_{\text{CORNER}}^{\text{Co}} = 19.9 \text{ kJ mol}^{-1}$ ,  $\varepsilon_{\text{EDGE}}^{\text{Co}} = 14.3 \text{ kJ mol}^{-1}$ ,  $\varepsilon_{\{100\}}^{\text{Co}} = 23.1 \text{ kJ mol}^{-1}$  and  $\varepsilon_{\{111\}}^{\text{Co}} = 11.4 \text{ kJ mol}^{-1}$ . Using the procedures described in the literature [73], the accuracy of the method was estimated to be  $5 \text{ kJ mol}^{-1}$  and its precision (evaluated on a test set of 10  $\text{Co}_{58}\text{Ni}_{58}$  structures not included in the fitting) was estimated to be  $25 \text{ kJ mol}^{-1}$ .

The structure of the obtained  $\text{Co}_{58}\text{Ni}_{58}$  with the lowest energy chemical ordering reflects the relative values of the descriptors. For instance, in the structure with the lowest DFT energy (Fig. 3),

all corner sites and (100) terrace sites are occupied by Ni because of the notably positive (~endothermic) energy of the respective descriptors around  $20 \text{ kJ mol}^{-1}$ . In turn, Co is present at the edge sites,  $2/24$  sites = 8%, and at (111) terrace sites,  $18/24$  = 75%, because their descriptors are less positive,  $\sim 13 \text{ kJ mol}^{-1}$ . The remaining 38 Co atoms compose 100% of the NP bulk. Finally, the slightly exothermic energy of Co-Ni heteroatomic bond formation,  $\varepsilon_{\text{BOND}}^{\text{Ni-Co}} = -0.2 \text{ kJ mol}^{-1}$ , favors mixing between Co and Ni, but, due to its low magnitude, the formation of a Co-core/Ni-shell structure would occur at equilibrium at absolute zero.

Since experimentally prepared catalysts contain significantly larger nanoparticles than  $\text{Co}_{58}\text{Ni}_{58}$ , we extended our simulations to larger species as well. Namely, we applied the obtained descriptors to determine the most thermodynamically stable chemical order in truncated octahedral  $\sim 3.6$  nm large  $\text{Co}_{719}\text{Ni}_{720}$  particles. The transferability of descriptors between NP of different sized but similar composition has been convincingly demonstrated before [73–75]. For the larger particles, we calculated a representative chemical ordering at absolute zero (i.e., the lowest energy structure) and at 1000 K, which is close to the reaction temperature of DRM. For simulations at 1000 K we account for thermal disordering of the alloy through a Metropolis Monte-Carlo approach. Whereas the surface at absolute zero is entirely covered by Ni, the surface of the structure at 1000 K consists of 30% Co (see Fig. 3) due to the entropic disorder introduced at high temperature. Nevertheless, even at 1000 K, only a minor fraction of the edge and terrace sites, 25% and 32%, respectively, are occupied by Co. This means that Co atoms do not occupy the Ni edges preferentially, in contrast to potassium, sulfur and gold [18], and hence, the alloying Co with Ni affects the catalytic performance in a different way. The enrichment of the surface by Ni at lower temperature is consistent with the measurements on Co-Ni single crystals annealed at high temperature in vacuum [78]. The observed difference between the measured segregation energy of  $17.4 \pm 1.6 \text{ kJ mol}^{-1}$  on (111) surface and the calculated  $\varepsilon_{\{111\}}^{\text{Co}} = 11.4 \text{ kJ mol}^{-1}$  can be explained by

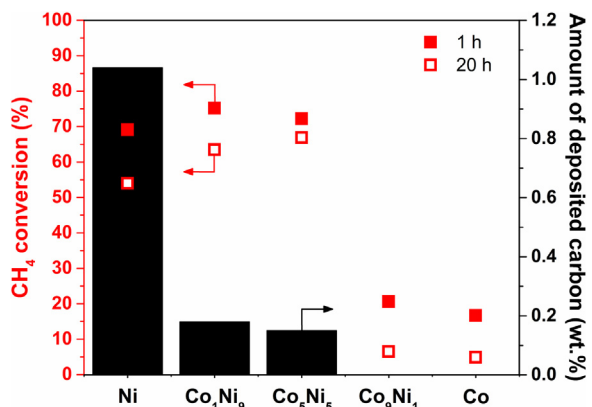


**Fig. 4.** CH<sub>4</sub> conversion at 1 and 20 h time on stream and amounts of deposited carbon after 20 h for the DRM at 750 °C using CoNi/ZrO<sub>2</sub> catalysts with various CoNi ratios (50 mg, 10 kPa CH<sub>4</sub> and 10 kPa CO<sub>2</sub>, GHSV = 1201 h<sup>-1</sup> g<sup>-1</sup>).

the approximate treatment of the temperature effects in the simulations and the imperfect description of the surface energies by the exchange correlation functional [79].

### 3.2. Catalytic behavior and catalyst structure during DRM

DRM reaction was conducted over the CoNi/ZrO<sub>2</sub> catalysts with different Co/Ni ratios (0:10, 1:9, 5:5, 9:1, 10:0) to examine the influence of the metal identity of the CoNi bimetallic system on catalytic rate, stability and carbon deposition. The time on stream data for CH<sub>4</sub> and CO<sub>2</sub> conversions and H<sub>2</sub>/CO ratios over CoNi/ZrO<sub>2</sub> with different Co/Ni ratios are demonstrated in Figs. S9, S1. The representative summary is shown in Fig. 4, demonstrating CH<sub>4</sub> conversions at 1 and 20 h time on stream of DRM at 750 °C. The difference in the conversions reflects the stability of the catalysts. The monometallic Ni catalyst shows relatively high initial conversion (69%), which gradually decreased to 54% after 20 h of the reaction. Substituting small quantity of Co (Co<sub>1</sub>Ni<sub>9</sub>) maintained high conversion level with gradual mild deactivation (75% to 64%). The catalytic stability was improved when unimolar of Co and Ni was present (Co<sub>1</sub>Ni<sub>1</sub>) while maintaining high conversion level (72% to 67%). When the amount of Co was increased (Co<sub>9</sub>Ni<sub>1</sub>), the conversion decreased from the initial stage of the reaction with further decrease with time (21% to 7%). Monometallic Co catalyst showed also low conversion with substantial decrease in conversions (17% to 5%). The slightly higher conversions of Co<sub>1</sub>Ni<sub>9</sub> and Co<sub>1</sub>Ni<sub>1</sub> samples than that of monometallic Ni can be partially explained by larger amount of available surface areas for Co<sub>1</sub>Ni<sub>9</sub> and Co<sub>1</sub>Ni<sub>1</sub> samples than monometallic Ni, as seen from Table 2. We therefore consider that partial substitution of Co did not drastically alter the reactivity of Ni, consistent with DFT expectation exhibiting richer Ni surface atoms on CoNi alloy particles, as demonstrated in Fig. 3.

The amounts of deposited carbon on the catalysts after 20 h of DRM were measured by TPO. The amounts are also shown in Fig. 4. The C amounts were 1.04, 0.18, 0.15, <0.01, and <0.01 wt.% for the Ni, Co<sub>1</sub>Ni<sub>9</sub>, Co<sub>5</sub>Ni<sub>5</sub>, Co<sub>9</sub>Ni<sub>1</sub> and Co catalysts, respectively. The monometallic Ni catalyst shows substantial amount of deposited carbon after the reaction, suggesting the formation of whisker-type carbon with high C/metal ratio [1]. When small quantity of Co was substituted with Ni, the drastic suppression of carbon was observed. The sample with an equimolar Co and Ni showed low amount of deposited carbon. Interestingly, high loading of Co (Co<sub>9</sub>Ni<sub>1</sub> and monometallic Co samples) showed negligible deposited carbon, suggesting that the cause of deactivation was not carbon encapsulation of the active metal surface. By combining catalytic results and carbon quantification results, there seems to be an optimum Co/Ni ratio that exhibits high conversion while

suppressing carbon deposition. In this study, an equimolar Co<sub>5</sub>Ni<sub>5</sub> sample (hereafter denoted simply as CoNi catalyst) improved both DRM stability and high tolerance towards carbon formation. In the following sections of this paper, it was attempted to monitor the structural changes *in-operando* during the DRM catalysis for three representative catalysts (Co, CoNi, and Ni catalysts) and to give a reasonable explanation for these differences.

*In-operando* XAS measurements were used to capture the structural changes of the metals during the DRM. After switching the effluent to a DRM reaction mixture, the CH<sub>4</sub> and CO<sub>2</sub> conversions were monitored by mass spectroscopy (Fig. S10) well reproducing the results shown in Fig. S9. XANES and EXAFS spectra were taken at regular intervals during 10 h. The key finding is illustrated on Fig. 5, which shows the Co K-edge XANES spectra taken after 0, 5, 60, and 600 min of DRM reaction for the monometallic Co and bimetallic CoNi catalysts. The first XANES spectrum taken after 5 min shows a small increase in the white line and a decrease in the pre-edge intensity for both catalysts. Linear combination using the spectra recorded at 750 °C for a fully reduced and a fully oxidized catalyst with a CO<sub>2</sub>:He mixture (1:9) indicates that 85% and 89% of the Co atoms remain reduced in Co and CoNi. Considering the dispersion of the NPs (17% (Co) and 20% (CoNi)) and assuming that Co oxidation occurred only at the metal surface during the first 5 min, the oxygen coverages ( $\theta_{\text{Co}-\text{O}}$ ) were 0.89 (Co) and 0.55 (CoNi). A comparison of the final states of the Co and Ni atoms for all catalysts is shown in Fig. 2. After 10 h of reaction, the total amount of metallic Co noticeably decreased for Co (74%) and slightly decreased for the CoNi catalyst (85%). This finding suggests that the bulk of the Co NPs was progressively oxidized in Co during the course of the reaction, while further oxidation in the CoNi catalyst remained minor. Moreover, no substantial oxidation of Ni atoms and no formation of Ni carbide was detected in the Ni and CoNi catalysts when examining the spectra recorded at the Ni K-edge (Fig. 2 and Fig. S11).

Qualitative assessment of the Co K-edge EXAFS spectra for two Co-based catalysts after 10 h of reaction shows a slight modulation of the oscillations around  $k \approx 4 \text{ \AA}^{-1}$  due to the presence of a light backscatterer (Fig. 2b). This is more evident for the Co catalyst in the FT-EXAFS spectrum, which shows a shoulder on the left-hand side of the Co-metal scattering path (Fig. 2d). Hence, the models for the EXAFS fitting of the Co and CoNi catalysts after 10 h of DRM reaction include the relevant metal–metal scattering paths, completed based on an additional metal–oxygen scattering path, to quantify Co oxidation. For Ni-based catalysts, no significant change in the Ni K-edge was observed, so only a single Ni–Ni scattering path was used. For Ni catalyst, a slight increase in the coordination number of the Ni–Ni bond was found after the reaction (9 ± 2 vs. 11 ± 2), which suggests an increase in the NP size (Table 1). For the Co catalyst, the coordination numbers of the Co–Co and Co–O bonds were 7 ± 4 and 1.2 ± 0.6, respectively, confirming the partial oxidation of the NP bulk (Table 1). For the CoNi catalyst, the first coordination spheres of Ni and Co were, respectively, fitted with 10 ± 1 and 7 ± 1 metal atoms and 0.7 ± 0.2 additional oxygen atom in the first coordination shell of Co. Firstly, the total coordination number of the metal–metal bonds was 8.5 before and after the reaction, which indicates that the particle size is stable after 10 h of reaction. Secondly, the coordination number of the Co–metal bond decreased after 10 h of DRM (Table 1), providing evidence of Co segregation towards the NP surface. Thirdly, the EXAFS quantitative analysis of the CoNi catalyst highlighted the slight oxidation of the Co metal. The driving force inducing Co segregation was thus attributed to oxidation occurring on the NP surface.

According to the XAS result, the main cause of deactivation for the Co catalyst was unambiguously assigned to metal oxidation. The successful detection of surface oxidation by XAS study was possible in this study because of the small particle sizes applied, in marked contrast to the previous XAS study in which no change

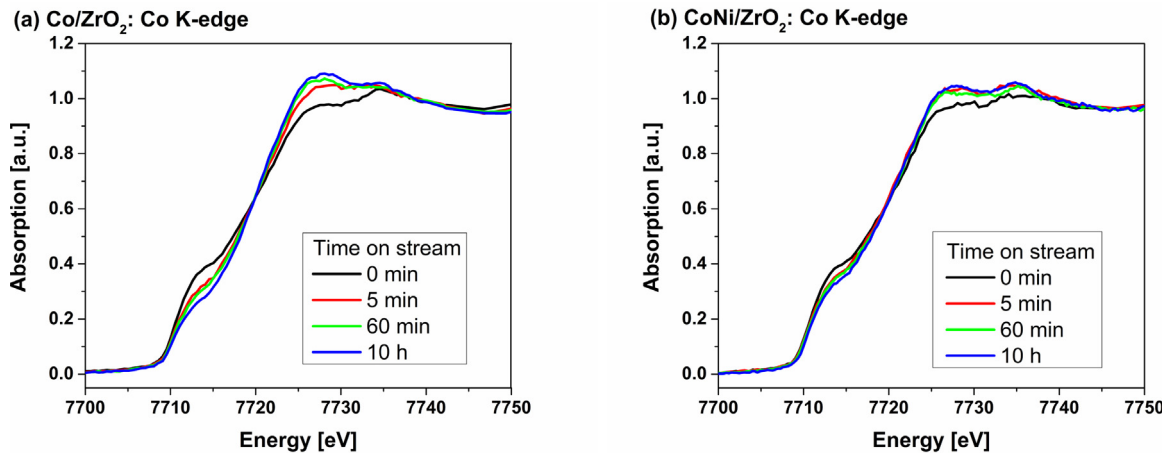
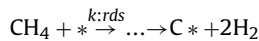


**Fig. 5.** Evolution of the XANES spectra at the Co K-edge for (a)  $\text{Co}/\text{ZrO}_2$  and (b)  $\text{Co}_{0.5}\text{Ni}_{0.5}/\text{ZrO}_2$  catalysts during the DRM.

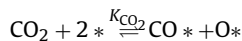
was observed in the oxidation state of metals during DRM when the large particles were used [41]. The CoNi catalyst showed a small quantity of deposited carbon, while maintaining the reduced state of the metal, consistent with being the least deactivated during the DRM (Fig. 4). The Ni catalyst had a larger amount of deposited carbon than the CoNi and Co catalysts. The inhibition of metal oxidation and carbon deposition by bimetallic CoNi may originate from kinetic control on the metal surface at steady-state DRM.

Detailed kinetic analysis at the low conversion level (<10%) was conducted for the three catalysts, after the initial rapid decay of the catalytic activity (~5 h). Drastic deactivation of the Co sample prevented accurate kinetic measurements at 750 °C, so the experiments were performed at a slightly higher temperature of 800 °C, where sufficiently stable performance was achieved (~5 h after the initial 5 h catalysis). The effects of the  $\text{CH}_4$  and  $\text{CO}_2$  partial pressures on the turnover rate of  $\text{CH}_4$  conversion were investigated. The turnover rates at varying  $\text{CH}_4$  pressures of 5–20 kPa and a constant  $\text{CO}_2$  pressure of 10 kPa are shown in Fig. 6a. In this range of pressures, the  $\text{CH}_4$  conversion rate increased in proportion to the  $\text{CH}_4$  pressure on all catalysts. This result is consistent with the C–H bond activation being the rate determining step, as reported for Ni catalysts by Wei and Iglesia [15]. The turnover rates were in the order of  $\text{Co} < \text{CoNi} < \text{Ni}$ , consistent with the literature for  $\text{TiO}_2$ -supported catalysts and the C–H bond activation capability.

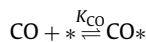
Distinct features were measured for the  $\text{CO}_2$  partial pressure dependence. The results of the turnover rates at varying  $\text{CO}_2$  pressures of 5–20 kPa at a constant  $\text{CH}_4$  pressure of 10 kPa are shown in Fig. 6b. The CoNi and Co catalysts showed negative order (~−0.5) with respect to the  $\text{CO}_2$  pressure. This result is in marked contrast with various Group VIII metals (Ni, Pt, Rh, Ru, etc.) where the turnover DRM rates are insensitive to  $\text{CO}_2$  pressures [15], and consistent with the recent discussion by Chin and co-workers for CoNi catalysts [80]. This kinetics indicates the occupation of  $\text{CO}_2$ -derived species (likely atomic oxygen), which compete with sites for  $\text{CH}_4$  activation. The plausible reaction sequence can be described as follows:  $\text{CH}_4$  is activated on the clean metal surface (1) as rate determining step (rds):



These sites are used to activate  $\text{CO}_2$  to leave surface  $\text{CO}^*$  and  $\text{O}^*$ :



The surface  $\text{CO}^*$  desorbs to gas phase:



The surface  $\text{O}^*$  should react with surface  $\text{C}^*$  which is formed as a result of  $\text{CH}_4$  activation (or CO disproportionation), to form CO. When the most abundant surface intermediate is  $\text{O}^*$ , the rate expression can be deduced as follows:

$$r = \frac{k [\text{CH}_4]}{1 + \frac{K_{\text{CO}_2} [\text{CO}_2]}{K_{\text{CO}} [\text{CO}]}}$$

For the Ni sample, the turnover rate was independent of the  $\text{CO}_2$  pressure, suggesting that extent of  $\text{O}^*$  is small (the second term in the denominator  $\frac{K_{\text{CO}_2} [\text{CO}_2]}{K_{\text{CO}} [\text{CO}]}$  is negligibly smaller than 1). This result is consistent with that of Wei and Iglesia for a Ni catalyst measured at 600 °C [15]. Using their reported turnover rate and activation energy (~100 kJ mol<sup>−1</sup>), the turnover rate expected at 800 °C for both  $\text{CH}_4$  and  $\text{CO}_2$  was ~10 s<sup>−1</sup> at 10 kPa. The observed rate in this study was ~4.5 s<sup>−1</sup>, which we consider to be within the experimental error originating from kinetic measurements and metal dispersion estimation.

The negative kinetic order in  $\text{CO}_2$  for the catalyst containing Co originates from the chemisorption capability associated with the oxophilic nature. The chemisorption energies of the products of  $\text{CO}_2$  dissociation, O atoms and CO molecules on the monometallic Ni and Co and bimetallic CoNi were estimated using DFT calculations. Consistent with the structures of the experimental samples, we investigated the adsorption on Ni, Co and CoNi with fcc crystal lattices. Since the size of  $\text{Co}_{0.5}\text{Ni}_{0.5}/\text{ZrO}_2$  particles considered for the optimization of CoNi chemical ordering at 1000 K impedes its explicit DFT calculation, we used the slab approach (Fig. 7). We considered the (111) surface of the Co-Ni alloy since it is the most stable surface for Ni, Co and other transition metals [81–83]. For monometallic Ni and Co, a 6-layer p(4 × 4) slab was built. For CoNi, a representative CoNi(111) slab was cut from one of the {111} terraces of the  $\text{Co}_{0.5}\text{Ni}_{0.5}/\text{ZrO}_2$  representative particle structure at 1000 K. The 6-layer p(4 × 4) slab consisted of 40 Ni and 56 Co atoms with 11 Ni and 5 Co atoms located on the slab surface. In line with the available experimental data, we studied the adsorption of CO and O on the fcc and hcp three-fold hollow sites of all three catalysts. Whereas on pure Ni(111) and Co(111) surfaces, all fcc and hcp sites were equivalent, on the Co-Ni(111) surface, all 16 fcc and 16 hcp sites in the p(4 × 4) cell were considered (Fig. 7 and Table S1).

The CO adsorption energy on Co and Ni was 150 and 156 kJ mol<sup>−1</sup> on the fcc sites, respectively, and 160 kJ mol<sup>−1</sup> on the hcp sites for both metals. The average adsorption energy calculated on the 16 fcc and 16 hcp sites of CoNi was  $160 \pm 16$  kJ mol<sup>−1</sup>, indicating that CO adsorption remains essentially unchanged upon alloying. In contrast, O atoms were adsorbed significantly stronger on the

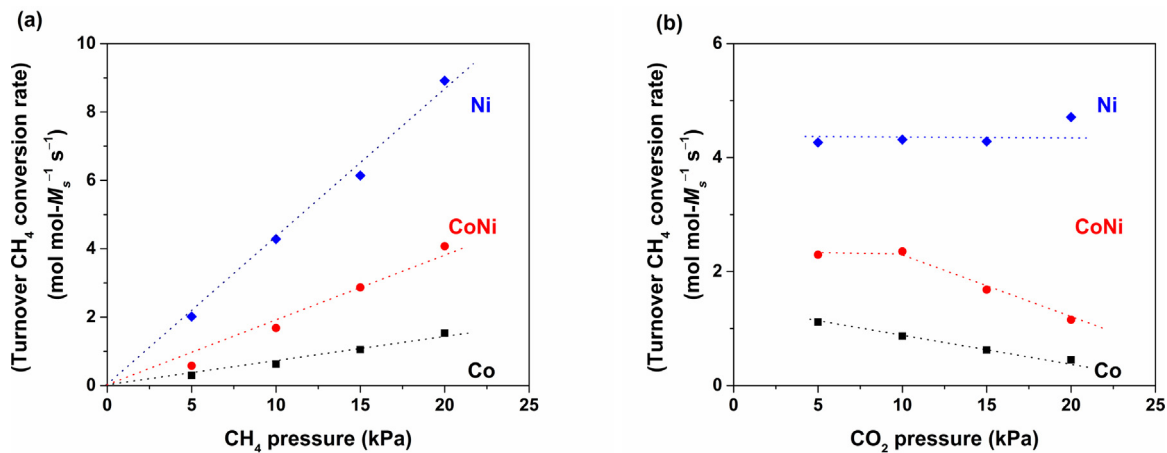


**Fig. 6.** Effects of the (a)  $\text{CH}_4$  and (b)  $\text{CO}_2$  partial pressure on the  $\text{CH}_4$  reaction rate for DRM on Ni, CoNi and Co catalysts supported on zirconia (800 °C, 10 kPa  $\text{CH}_4$  or  $\text{CO}_2$ , balance Ar).

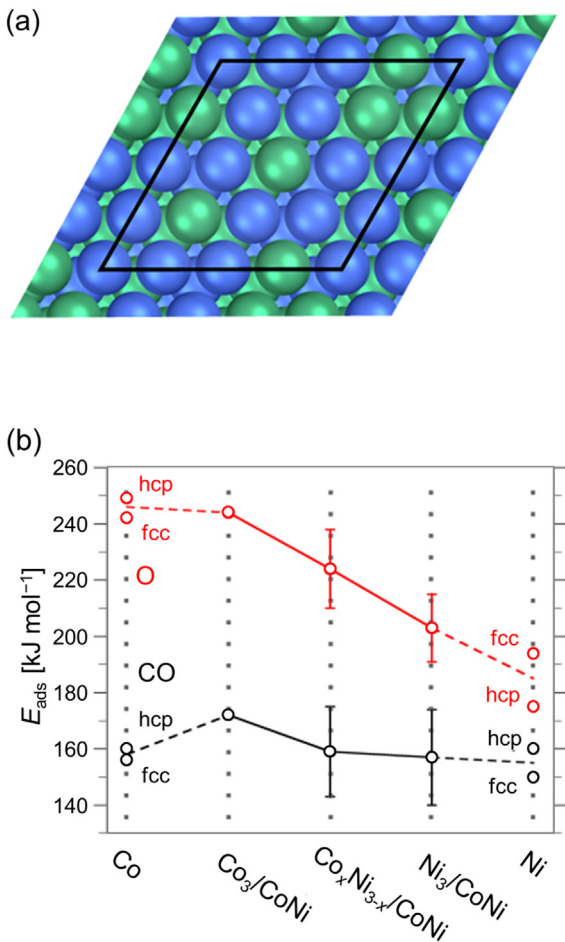


**Fig. 7.** Co-Ni surface employed in the calculations of CO and O adsorption at the top and the calculated adsorption energies on fcc-Co(111), sites with various composition on CoNi(111) and Ni(111) surfaces at the bottom. Average values of the adsorption energies are also given. See Fig. S12 and Table S1 for individual adsorption energies.

Co(111) surface ( $\sim 245 \text{ kJ mol}^{-1}$ ), than on the Ni(111) (less than  $195 \text{ kJ mol}^{-1}$ ) (Table S1). The average adsorption energies of O on the 16 fcc and 16 hcp sites of the considered Co-Ni(111) surface were  $220 \pm 16 \text{ kJ mol}^{-1}$  and, as expected, it depends on the specific composition of the site. For example, the O adsorption energy on

the only fcc site composed of 3 Co atoms is  $244 \text{ kJ mol}^{-1}$ , which is very similar to the adsorption energy on the pure Co(111) surface. At the same time, O adsorption on the sites composed of 3 Ni atoms is somewhat weaker,  $203 \pm 12 \text{ kJ mol}^{-1}$ , which is very close to the adsorption energy on the pure Ni(111) surface. Consistently, O adsorption on 3-fold hollow sites composed of both Co and Ni atoms, with an average adsorption energy of  $224 \pm 14 \text{ kJ mol}^{-1}$ , is intermediate in strength between O adsorption on pure Ni(111) and Co(111) surfaces. The remarkably low average O adsorption energy on representative models of the CoNi(111) alloys provides an explanation for the experimental evidence, based on kinetic data and XAS analysis, that CoNi alloys are much less prone to oxidation than pure Co.

Finally, we briefly examined the issue of unwanted carbon formation on DRM catalysts by calculating adsorption energies of single C atoms. Considering that calculations on CO and O adsorption showed almost linear dependence of adsorption energies on the site composition, we limited these calculations to the pure Ni and Co surfaces. According to calculations, adsorption of C is only  $24 \text{ kJ mol}^{-1}$  stronger on Co (78 and  $98 \text{ kJ mol}^{-1}$  on the hcp and fcc sites) relative to Ni (111 and  $112 \text{ kJ mol}^{-1}$  on the hcp and fcc sites). This suggests that the two metals (and hence the alloy) have a similar tendency towards carbon formation, and that the reactivity tuning of CoNi alloy towards stable DRM is mainly ascribed to differences in O adsorption between Ni and Co.

Long-term stability test for the CoNi/ZrO<sub>2</sub> catalyst was conducted at 800 °C for more than 150 h. Fig. 8 shows the catalytic result. The CoNi bimetallic catalyst exhibited gradual but apparent deactivation with time. At  $\sim 165$  h, the catalyst was treated in H<sub>2</sub> and DRM was resumed. The catalytic activity was substantially recovered by H<sub>2</sub> treatment, suggesting that a part of the catalyst still suffered oxidation of metal relatively slowly during DRM, which could however be reactivated. Carbon amount after the reaction was only 0.16 wt%, clearly indicating that coke-tolerant nature of the CoNi catalyst. The activity loss that could not be recovered by H<sub>2</sub> treatment is reasonably ascribable to sintering of the metal particles, which requires another strategy to be suppressed. Indeed, further optimization was necessary to make the catalyst stabilized for even longer run. Possible approaches to overcome the issues are by optimizing reaction conditions leading to more reducible atmosphere [4], or by adding small amount of noble metal to the composition [29]. Simultaneously, this long-term testing results provide evidence that selecting bimetallic identities (Co vs. Ni) is possible to control the reactivity for the specific reaction, such as DRM.

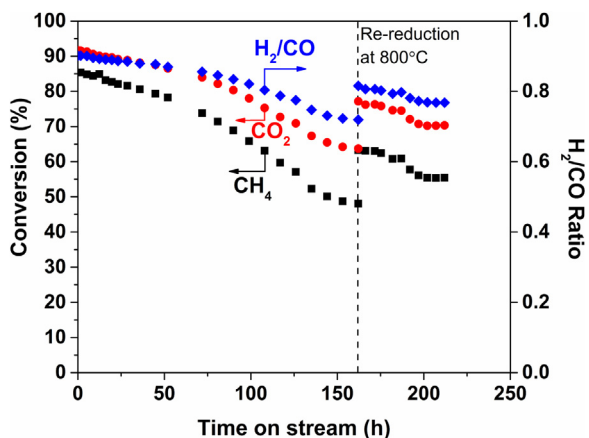


**Fig. 8.** Long-term test over CoNi/ZrO<sub>2</sub> catalyst for DRM (800 °C, 10 kPa CH<sub>4</sub> or CO<sub>2</sub>, balance Ar).

Overall, the combined results from *in-operando* XAS, the kinetic study, and DFT calculations allow to propose a consistent scenario for DRM on the Co-Ni surface. The conceptual scheme of the reaction pathway is presented in Fig. 9. For a pure Co surface, kinetically introduced and strongly bound O\* species (due to either relatively slow CH<sub>4</sub> activation or strong oxophilicity of the metal) caused site occupation for C–H bond activation of CH<sub>4</sub>. With time, oxidation gradually occurred from the surface of the metallic Co and proceeded to the bulk of the metal particles, as a consequence of the unbalanced kinetics of CH<sub>4</sub> and CO<sub>2</sub> activation. On pure Ni surfaces, the oxophilicity of pure Ni is insufficient for accumulation of O on the catalyst surface, which leaves the reduced metallic surface sites available for the CH<sub>4</sub> activation. Low coverage of the O\* species

leads to a slower removal of carbonaceous species formed through CH<sub>4</sub> decomposition (or CO disproportionation), resulting in the build-up of surface carbon. On the CoNi bimetallic surface at high temperature, the chemisorption enthalpy of O species is between that of its monometallic counterparts. The moderate oxophilicity of CoNi still causes a negative order in CO<sub>2</sub> pressure, suggesting that O\* formation competes with CH<sub>4</sub> activation. These O\* species, however, do not cause bulk oxidation of the CoNi metal due to either kinetic improvement of CH<sub>4</sub> activation (reduction reaction) over monometallic Co or thermodynamic tolerance to oxidation introduced by the coexistence of Ni atoms as DFT confirms. Overall, tuning the reactivity to balance the kinetics of CH<sub>4</sub> and CO<sub>2</sub> activation makes it possible to perform DRM without introducing O\* and C\* accumulation on the surface, i.e., oxidation of the metal and formation of carbon.

Recent DRM studies using bimetallic CoNi catalysts have focused on support materials with little attention given to the effects of the metal particle size. As discussed in the introduction, different supports often cause different metal dispersion and catalytic consequences. We would like to emphasize that, in this study, the metal dispersion was relatively high and comparable among the three catalysts: Ni, CoNi, and Co. This study therefore demonstrates the crucial role of metal reactivity towards two of the DRM reactants (CH<sub>4</sub> and CO<sub>2</sub>) to balance the redox capability on the metal surface. Tuning of the reactivity and resultant coke-suppression can be achieved by selecting an appropriate metal identity, especially an alloy of Co and Ni. This study did not fully elucidate the effects of the metal particle size and reaction temperature and pressure, which impact the reaction rate and the formation of carbon. The importance of step sites was emphasized in the literature, but the DFT calculation in this study did not show a preference of occupation of Co and Ni on the step sites by alloying. This study provides

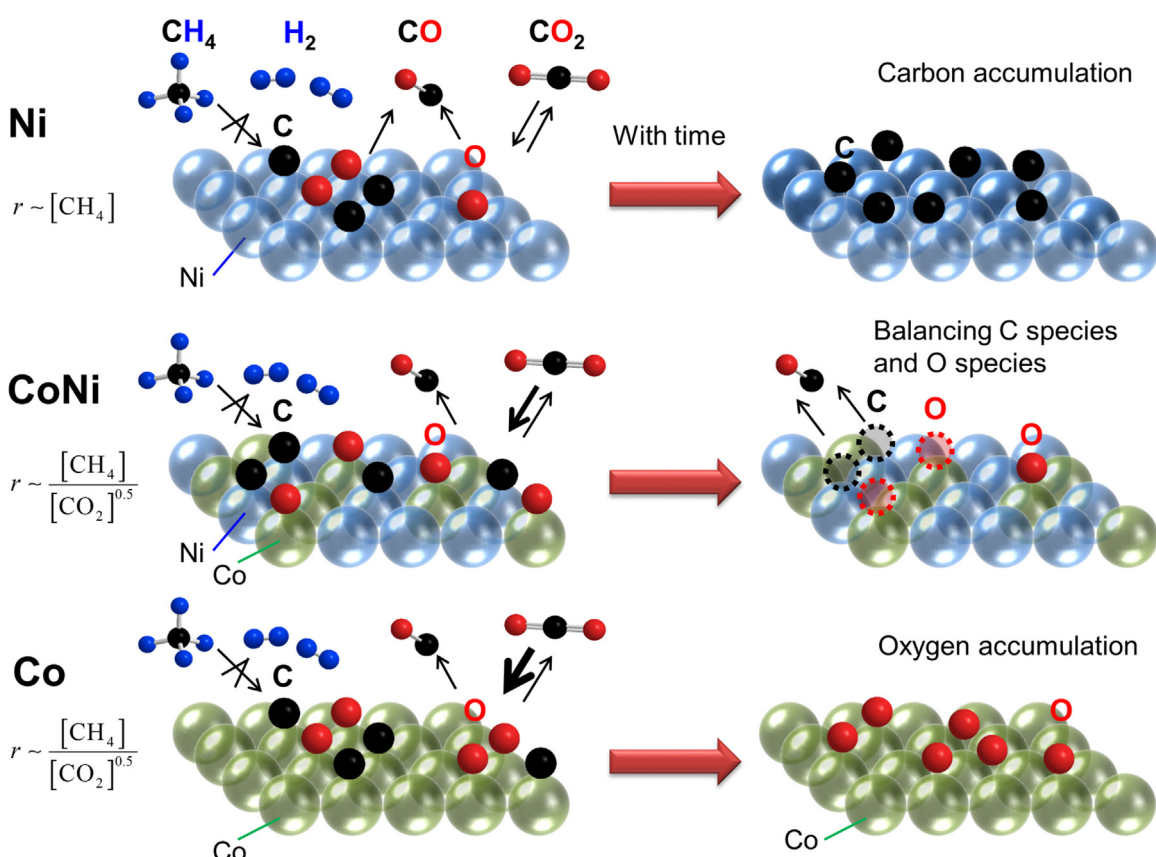


**Fig. 9.** Conceptual cartoon of the reactive surface for Ni, CoNi and Co during DRM reaction.

clear guidelines for future studies on reactivity tuning for coke-tolerant DRM with experimental evidence using *in-operando* XAS study, coupled with DFT calculations.

#### 4. Conclusions

The identity of a metal (Co, Ni and their alloy) can affect the reactivity towards CH<sub>4</sub> and CO<sub>2</sub> activation, resulting in different extents of steady-state coverage of surface oxygen species, mainly originating from CO<sub>2</sub>, for coke-tolerant DRM operation. By tuning CoNi ratios, stable catalytic performance with minimized carbon deposition was achieved for DRM. Both kinetic data and *in-operando* XAS showed that the pure Co resulted in richer oxygen coverage (negative order in CO<sub>2</sub>), while pure Ni maintained a reduced state and clean surface at the steady state (zero order in CO<sub>2</sub>). The XAS results provided further evidence of the oxidation of pure Co during DRM, which progressively occurred from the surface to the bulk with time. The Ni catalyst experienced carbon deposition, while the bimetallic CoNi catalyst showed negligible amount of deposited carbon, likely due to balancing the oxidative (CO<sub>2</sub>, H<sub>2</sub>O) and reductive (CH<sub>4</sub>, CO, H<sub>2</sub>) species reactions on the catalyst surface. DFT calculations showed that the CoNi metal surface had an intermediate energy of oxygen chemisorption, between those of monometallic Co and Ni. This study provides successful methodology to capture bimetallic catalysis using *in-operando* spectroscopic method, and its application to rationally design a catalyst with balanced kinetics for a given reaction.

#### Acknowledgments

This work was funded by Saudi Arabia Basic Industries Corporation (SABIC) through a collaborative research project with King Abdullah University of Science and Technology (KAUST). The authors gratefully thank Dr. Lawrence D'Souza (SABIC) for technical advice and valuable contributions. Moreover, the authors acknowledge Mr. Dong-Chang Kang, KAUST Catalysis Center, and Dr. Manuel A. Roldan-Gutierrez, KAUST Core Laboratories, for their assistance with the DRIFTS and TEM measurements, respectively. We are also grateful for the computational resources for the XAS spectra acquired from the KAUST Supercomputing Laboratory using the supercomputer Shaheen II under projects k1016 and k1133.

#### Appendix A. Supplementary data

Supplementary data associated with this article can be found, in the online version, at <http://dx.doi.org/10.1016/j.apcatb.2017.04.076>.

#### References

- [1] J.R. Rostrup-Nielsen, in: J.R. Anderson, M. Boudart (Eds.), *Catalysis, Science and Technology*, vol. 5, Springer Berlin, 1984, Chapter 1.
- [2] J.H. Lunsford, *Catal. Today* 63 (2000) 165–174.
- [3] S. Naito, *Catal. Surv. Jpn.* 4 (2000) 3–15.
- [4] K. Takanabe, *J. Jpn. Petrol. Inst.* 55 (2012) 1–12.
- [5] J.R. Rostrup-Nielsen, J.H.B. Hansen, *J. Catal.* 144 (1993) 38–49.
- [6] M. Bradford, M.A. Vannice, *Catal. Rev.* 41 (1999) 1–42.
- [7] Y.H. Hu, E. Ruckenstein, *Adv. Catal.* 48 (2004) 297–345.
- [8] J.-M. Lavoie, *Front. Chem.* 2 (2014) 81.
- [9] D. Pakhare, J. Spivey, *Chem. Soc. Rev.* 43 (2014) 7813–7837.
- [10] K. Mette, S. Kühl, A. Tarasov, M.G. Willinger, J. Kröhnert, S. Wrabetz, A. Trunschke, M. Scherzer, F. Girmsdies, H. Düdder, K. Kähler, K. Friedel Ortega, M. Muhler, R. Schlägl, M. Behrens, T. Lunkenbein, *ACS Catal.* 6 (2016) 7238–7248.
- [11] Z. Liu, D.C. Grinter, P.G. Lustemberg, T.-D. Nguyen-Phan, Y. Zhou, S. Luo, I. Waluyo, E.J. Crumlin, D.J. Stacchiola, J. Zhou, J. Carrasco, H.F. Busnengo, M.V. Ganduglia-Pirovano, S.D. Senanayake, J.A. Rodriguez, *Angew. Chem. Int. Ed.* 55 (2016) 7455.
- [12] S. Kawi, Y. Kathiraser, J. Ni, U. Oemar, Z. Li, E.T. Saw, *ChemSusChem* 8 (2015) 3556–3575.
- [13] M. Usman, W.M.A. Wan Daud, H.F. Abbas, *Renew. Sustain. Energy Rev.* 45 (2015) 710–744.
- [14] J. Sehested, J.A.P. Gelten, I.N. Remediakis, H. Bengaard, J.K. Nørskov, *J. Catal.* 223 (2004) 432–443.
- [15] J. Wei, E. Iglesia, *J. Catal.* 224 (2004) 370–383.
- [16] Y.H. Hu, E. Ruckenstein, *Catal. Rev.* 44 (2002) 423–453.
- [17] H.S. Bengaard, J.K. Nørskov, J. Sehested, B.S. Clausen, L.P. Nielsen, A.M. Molenbroek, J.R. Rostrup-Nielsen, *J. Catal.* 209 (2002) 365–384.
- [18] F. Besenbacher, I. Chorkendorff, B.S. Clausen, B. Hammer, A.M. Molenbroek, J.K. Nørskov, I. Stensgaard, *Science* 279 (1998) 1913–1915.
- [19] O. Yamazaki, K. Tomishige, K. Fujimoto, *Appl. Catal. A* 136 (1996) 49–56.
- [20] Z. Zhang, X.E. Verykios, *Appl. Catal. A* 138 (1996) 109–133.
- [21] M.C.J. Bradford, M.A. Vannice, *Appl. Catal.* 142 (1996) 73–96.
- [22] V.C.H. Kroll, H.M. Swaan, C. Mirodatos, *J. Catal.* 161 (1996) 409–422.
- [23] K. Nagaoka, K. Takanabe, K. Aika, *Chem. Commun.* (2002) 1006–1007.
- [24] E. Ruckenstein, H.Y. Wang, *J. Catal.* 205 (2002) 289–293.
- [25] K. Nagaoka, K. Takanabe, K. Aika, *Appl. Catal. A* 255 (2003) 13–21.
- [26] K. Takanabe, K. Nagaoka, K. Aika, *J. Catal.* 230 (2005) 75–85.
- [27] K. Takanabe, K. Nagaoka, K. Narai, K. Aika, *J. Catal.* 232 (2005) 268–275.
- [28] K. Takanabe, K. Nagaoka, K. Aika, *Catal. Lett.* 102 (2005) 153–157.
- [29] K. Nagaoka, K. Takanabe, K. Aika, *Appl. Catal. A* 268 (2004) 151–158.
- [30] J. Zhang, H. Wang, A.K. Dalai, *J. Catal.* 249 (2007) 300–310.
- [31] D. San-José-Alonso, J. Juan-Juan, M.J. Illán-Gómez, M.C. Román-Martínez, *Appl. Catal. A* 371 (2009) 54–59.
- [32] M.-S. Fan, A.Z. Abdullah, S. Bhatia, *Appl. Catal. B* 100 (2010) 365–377.
- [33] D. Liu, W.N.E. Cheo, Y.W.Y. Lim, A. Borgna, R. Lau, Y. Yang, *Catal. Today* 154 (2010) 229–236.
- [34] M.S. Fan, A.Z. Abdullah, S. Bhatia, *ChemSusChem* 4 (2011) 1643–1653.
- [35] S.Y. Foo, C.K. Cheng, T.-H. Nguyen, A.A. Adesina, *Catal. Today* 164 (2011) 221–226.
- [36] A. Horváth, G. Stefler, O. Geszti, A. Kienneman, A. Pietraszek, L. Guczi, *Catal. Today* 169 (2011) 102–111.
- [37] H. Liu, R. Zhang, R. Yan, B. Wang, K. Xie, *Appl. Surf. Sci.* 257 (2011) 8955–8964.
- [38] M. Zhao, T.L. Church, A.T. Harris, *Appl. Catal. B* 101 (2011) 522–530.
- [39] I.O. Črnivec, P. Djinović, B. Erjavec, A. Pintar, *Chem. Eng. J.* 207 (2012) 299–307.
- [40] P. Djinović, I.G.O. Črnivec, B. Erjavec, A. Pintar, *Appl. Catal. B* 125 (2012) 259–270.
- [41] V.M. Gonzalez-delaCruz, R. Pereniguez, F. Ternero, J.P. Holgado, A. Caballero, *J. Phys. Chem. C* 116 (2012) 2019–2926.
- [42] I. Luisetto, S. Tutti, E. Di Bartolomeo, *Int. J. Hyd. Energy* 37 (2012) 15992–15999.
- [43] A.G. Bhavani, W.Y. Kim, J.Y. Kim, J.S. Lee, *Appl. Catal. A* 450 (2013) 63–72.
- [44] K. Li, M. Jiao, Y. Wang, Z. Wu, *Surf. Sci.* 617 (2013) 149–155.
- [45] N. Rahemi, M. Haghighi, A.A. Babaloo, M.F. Jafari, S. Allahyari, *Catal. Sci. Technol.* 3 (2013) 3183–3191.
- [46] H. Wang, J.T. Miller, M. Shakouri, C. Xi, T. Wu, H. Zhao, M.C. Akatay, *Catal. Today* 207 (2013) 3–12.
- [47] M.S. Aw, M. Zorko, P. Djinović, A. Pintar, *Appl. Catal. B* 164 (2015) 100–112.
- [48] X. Fan, Z. Liu, Y.-A. Zhu, G. Tong, J. Zhang, C. Engelbrekt, J. Ulstrup, K. Zhu, X. Zhou, *J. Catal.* 330 (2015) 106–119.
- [49] J. Wei, E. Iglesia, *J. Phys. Chem. B* 108 (2004) 4094–4103.
- [50] M.K. van der Lee, A.J. van Dillen, J.H. Bitter, K.P.J. de Jong, *J. Am. Chem. Soc.* 127 (2005) 13573–13582.
- [51] K. Tamura, M. Inui, S. Hosokawa, *Rev. Sci. Instrum.* 66 (1995) 1382–1384.
- [52] B. Ravel, M. Newville, *J. Synchrotron Rad.* 12 (2005) 537–541.
- [53] A.L. Ankudinov, J. Rehr, *J. Phys. Rev. B* 56 (1997) 1712–1715.
- [54] B.W. Lee, R. Alsenz, A. Ignatiev, M.A. Van Hove, *Phys. Rev. B* 17 (1978) 1510–1520.
- [55] A.S. Andreev, J.-B. d'Espinose de La Caillerie, O.B. Lapinaa, A. Geraschenko, *Phys. Chem. Chem. Phys.* 17 (2015) 14598–14604.
- [56] B. Predel, *Phase Equilibria, Crystallographic and Thermodynamic Data of Binary Alloys' of Landolt-Börnstein-Group IV Physical Chemistry*, in: O. Modeling (Ed.), Springer-Verlag, Berlin, 1993.
- [57] G. Kresse, J. Furthmüller, *Phys. Rev. B* 54 (1996) 11169–11186.
- [58] B. Hammer, L. Hansen, J. Nørskov, *J. Phys. Rev. B* 59 (1999) 7413–7421.
- [59] M. Methfessel, A.T. Paxton, *Phys. Rev. B* 40 (1989) 3616–3621.
- [60] G. Kresse, D. Joubert, *Phys. Rev. B* 59 (1999) 1758–1775.
- [61] F. de Groot, G. Vankó, P. Glatzel, *J. Phys. Condens. Matter* 21 (2009) 104207.
- [62] D. Cabaret, A. Bordage, A. Juhin, M. Arfaoui, E. Gaudry, *Phys. Chem. Chem. Phys.* 12 (2010) 5619–5633.
- [63] A.I. Frenkel, C.W. Hills, R.G. Nuzzo, *J. Phys. Chem. B* 105 (2001) 12689–12703.
- [64] R.B. Greecor, F.W. Lytle, *J. Catal.* 63 (1980) 476–486.
- [65] E.A. Owen, E.L. Yates, *Phil. Mag.* 21 (1936) 809–819.
- [66] S. In-Kook, H. Ohta, Y. Waseda, *J. Mater. Sci.* 23 (1988) 757–760.
- [67] L. Marick, *Phys. Rev.* 49 (1936) 831–837.
- [68] E.A. Owen, D. Madoc Jones, *Proc. Phys. Soc. B* 67 (1954) 456–466.
- [69] G. Apai, J.F. Hamilton, J. Stohr, A. Thompson, *Phys. Rev. Lett.* 43 (1979) 165–169.
- [70] L.B. Hansen, P. Stoltze, J.K. Nørskov, B.S. Clausen, W. Niemann, *Phys. Rev. Lett.* 64 (1990) 3155–3158.
- [71] B.S. Clausen, L. Græbaek, H. Topsøe, L.B. Hansen, P. Stoltze, J.K. Nørskov, *J. Catal.* 141 (1993) 368–379.
- [72] B.J. Clausen, H. Topsøe, L.B. Hansen, P. Stoltze, J.K. Nørskov, *Jpn. J. Appl. Phys.* 32 (1993) 95–97.
- [73] S.M. Kozlov, G. Kovács, R. Ferrando, K.M. Neyman, *Chem. Sci.* 6 (2015) 3868–3880.

- [74] M. Vorokhta, I. Khalakhan, M. Václavú, G. Kovács, S.M. Kozlov, P. Kúš, T. Skála, N. Tsud, J. Lavková, V. Potin, I. Matolínová, K.M. Neyman, V. Matolín, *Appl. Surf. Sci.* 365 (2016) 245–251.
- [75] G. Kovács, S.M. Kozlov, I. Matolínová, M. Vorokhta, V. Matolín, K.M. Neyman, *Phys. Chem. Chem. Phys.* 17 (2015) 28298–28310.
- [76] A. Neitzel, G. Kovács, Y. Lykhach, S.M. Kozlov, N. Tsud, T. Skála, M. Vorokhta, V. Matolín, K.M. Neyman, J. Libuda, *Top. Catal.*, in press, 10.1007/s11244-016-0709-5.
- [77] A. Wolfbeisser, G. Kovács, S.M. Kozlov, K. Föttinger, J. Bernardi, B. Klötzer, K.M. Neyman, G. Rupprechter, *Catal. Today* 283 (2017) 134–143.
- [78] E.E. Hajcsar, P.R. Underhill, W.W. Smeltzer, P.T. Dawson, *Surf. Sci.* 191 (1987) 249–258.
- [79] P. Janthon, S.M. Kozlov, F. Viñes, J. Limtrakul, F. Illas, *J. Chem. Theory Comput.* 9 (2013) 1631–1640.
- [80] W. Tu, M. Ghoussooub, C.V. Singh, Y.-H. Chin, OA16, The 16th International Congress on Catalysis, Beijing, 2016.
- [81] G. Kresse, J. Hafner, *Surf. Sci.* 459 (2000) 287–302.
- [82] F. Mittendorfer, A. Eichler, J. Hafner, *Surf. Sci.* 423 (1999) 1–11.
- [83] A. Dannenberg, M.E. Gruner, A. Hucht, P. Entel, *Phys. Rev. B* 80 (2009) 1–15.